

Supporting Information

Metal-Organic Frameworks Mediate Cu Coordination for Selective CO₂

Electroreduction

*Dae-Hyun Nam,[†] Oleksandr S. Bushuyev,[†] Jun Li,^{†,‡} Phil De Luna,^{†,§} Ali Seifitokaldani,[†]
Cao-Thang Dinh,[†] F. Pelayo García de Arquer,[†] Yuhang Wang,[†] Zhiqin Liang,[†]
Andrew H. Proppe,^{†,||} Chih Shan Tan,[†] Petar Todorović,[†] Osama Shekhah,[⊥]
Christine M. Gabardo,[‡] Jea Woong Jo,[†] Jongmin Choi,[†] Min-Jae Choi,[†] Se-Woong Baek,[†]
Junghwan Kim,[†] David Sinton,[‡] Shana O. Kelley,^{||,#} Mohamed Eddaoudi,[⊥]
and Edward H. Sargent^{*,†}*

[†]Department of Electrical and Computer Engineering, University of Toronto, 10 King's College Road, Toronto, Ontario M5S 3G4, Canada

[‡]Department of Mechanical and Industrial Engineering, University of Toronto, 5 King's College Road, Toronto, Ontario M5S 3G8, Canada

[§]Department of Materials Science and Engineering, University of Toronto, 184 College Street, Toronto, Ontario M5S 3E4, Canada

^{||} Department of Chemistry, University of Toronto, 80 St. George Street, Toronto, Ontario M5S 3G4, Canada

[⊥]Division of Physical Sciences and Engineering, Advanced Membranes and Porous Materials Center, Functional Materials Design, Discovery and Development Research Group (FMD³), King Abdullah University of Science and Technology (KAUST), Thuwal 23955-6900, Kingdom of Saudi Arabia

[#]Department of Pharmaceutical Sciences, Leslie Dan Faculty of Pharmacy, University of Toronto, 144 College Street, Toronto, Ontario M5S 3M2, Canada

1. EPR analysis of CuAc

The EPR signal of CuAc as well as HKUST-1 was measured to investigate the effect of MOF structure on the calcination-induced Cu dimer structure modulation (Figure S6). In contrast to HKUST-1, there was no obvious tendency of electron configuration modulation in Cu dimer of CuAc according to the degree of thermal treatment. Compared to as-prepared CuAc, the EPR center peak was shifted toward the lower magnetic field, and the signal intensity decreased after 200°C calcination. As the CuO started to be generated at an increased isothermal time of 200°C calcination, the EPR signal disappeared gradually.

2. In situ EXAFS of HKUST-1

To track the Cu cluster formation from a Cu dimer, we plotted a 3D map of the in situ EXAFS signal during the first 9 ~ 90 s of reaction (Figure S11). In Figure 4, the Cu-O peak of $|\chi(R)|$ in the 'before reaction' status of HKUST-1 indicates the Cu dimer (Cu 2+) at the MOF node. At the reaction time of 90 s, the Cu-Cu peak intensity increased with decreasing Cu-O peak intensity. This Cu-Cu peak is maintained during the CO₂RR. In Figure S11, we can see the process of Cu cluster formation from the Cu dimer. In as-prepared HKUST-1, the intensity of Cu-O peak diminished at 60 s and the intensity of Cu-Cu peak increased simultaneously. Interestingly, 250°C 3 h and 10 h calcined HKUST-1 showed the lower Cu-Cu peak intensity of $|\chi(R)|$ compared to as-prepared HKUST-1. This change in Cu-Cu peak intensity is related to the lower Cu-Cu CN number during the CO₂RR.

3. CO₂RR stability of HKUST-1

We report a study of CO₂RR stability of 250°C 3 h calcined HKUST-1, which exhibited the highest C₂H₄ FE of 45%. Figure S28 is the chronoamperometry and gaseous product analysis of CO₂RR

as a function of reaction time in a flow cell. HKUST-1 showed good CO₂RR stability with high current density (J) in flow cell. Over the first 140 minutes, C₂H₄ FE was stable in the range of 42 ~ 45% and H₂ FE did not increase over 8%. After 140 min, the gas diffusion layer (GDL) lost hydrophobicity and the gas cathode chamber flooded with electrolyte, compromising the C₂H₄ FE. In flow cells, carbon-based GDLs, which enable CO₂ diffusion toward the catalyst, provide cell operation with high current under alkaline conditions. The GDL can degrade during CO₂RR because the GDL surface loses hydrophobicity and becomes hydrophilic, as previously reported.⁷

As a result, in order to investigate the CO₂RR stability of the HKUST-1 electrocatalyst for a longer time, we measured CO₂RR stability of 250°C 3 h calcined HKUST-1 in H-cell (Figure S28b). Due to the limited pH range of electrolyte (pH <10) in H-cell, 0.1M KHCO₃ was used as an electrolyte and an applied potential was changed for the performance optimization. Compared to flow cell, HKUST-1 in H-cell showed lower C₂H₄ FE (37 ~ 42%) and higher H₂ FE 14%. The reaction exhibited stable H-cell operation in CO₂-saturated 0.1M KHCO₃ at -2.4 V vs. Ag/AgCl (-1.8 V vs. RHE, non-iR corrected) over 460 minutes of operation.

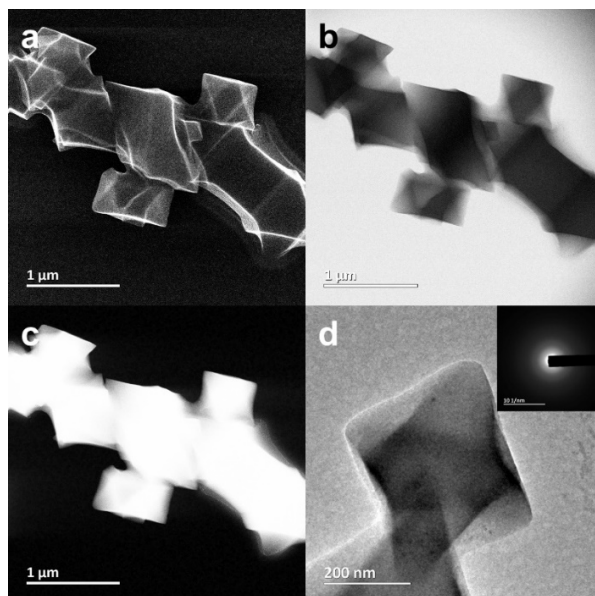


Figure S1. (a) SEM, (b) TEM bright field, (c) TEM HAADF image of as-fabricated HKUST-1 powders, and (d) highly magnified TEM image of octahedral HKUST-1 with the diffraction pattern.

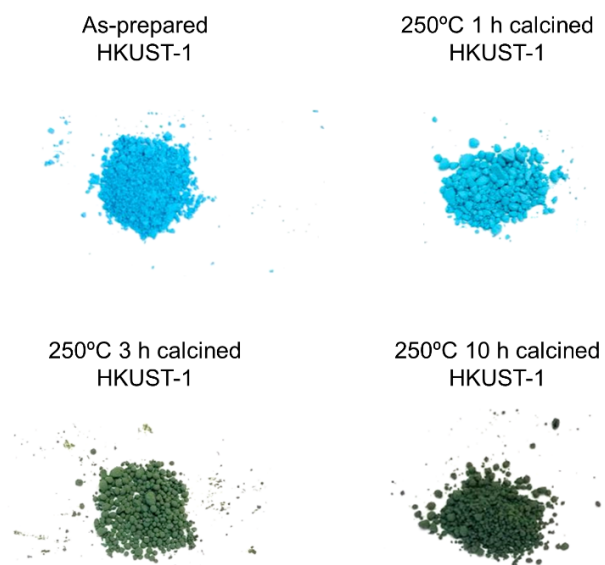


Figure S2. HKUST-1 powders (as-prepared, 250°C 1 h, 3 h, 10 h calcination) fabricated in this work. The color of HKUST-1 changes from light blue to dark green as the degree of thermal calcination increases.

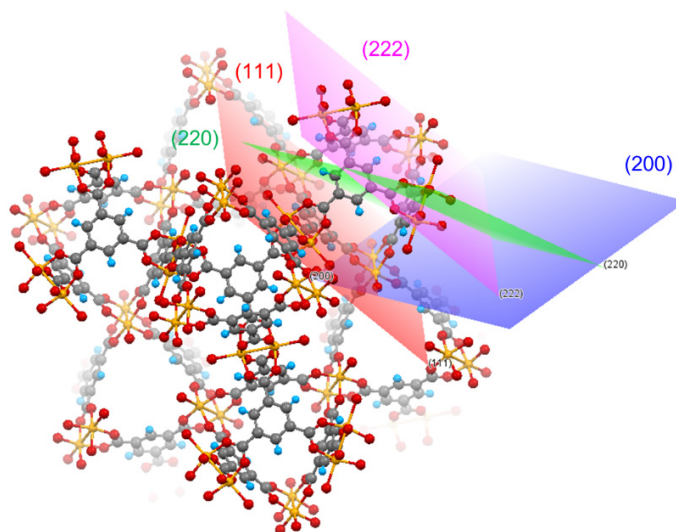


Figure S3. Schematic for displaying the position of calculated (111), (200), (220), and (222) plane in HKUST-1

Table S1. XRD peak position of (111), (200), (220), and (222) plane of HKUST-1 according to the isothermal time at 250°C calcination.

	XRD peak position (°) of plane			
	(111)	(200)	(220)	(222)
Simulated HKUST-1	5.82	6.72	9.50	11.64
As-prepared HKUST-1	5.62	6.62	9.40	11.50
250°C 1 h HKUST-1	5.99	6.92	9.74	11.81
250°C 3 h HKUST-1	.	6.42	9.20	11.26
250°C 10 h HKUST-1	.	6.46	9.08	11.18

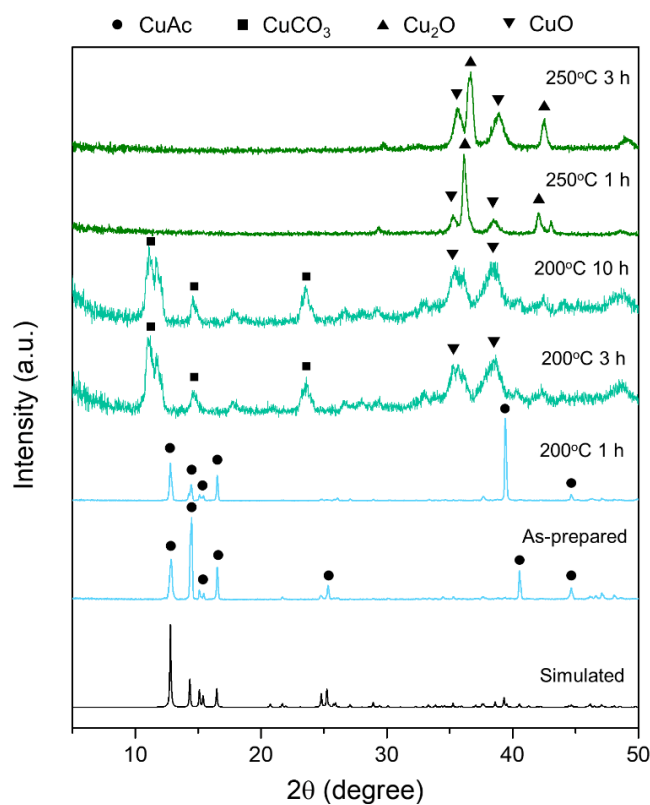


Figure S4. XRD analysis for investigating the phase transition of CuAc according to the calcination temperatures of 200°C, 250°C and related isothermal time of 1, 3, 10 h. CuAc phase was maintained until 200°C 1 h calcination. CuCO₃ phase was formed at 200°C 3 h and 200°C 10 h calcination. 250°C 1 h and 3 h condition induced the mixed phase of CuO + Cu₂O after calcination. Compared to HKUST-1, CuAc showed lower thermal decomposition temperature.

Table S2. Calculated EPR parameters of HKUST-1 from fitted spectra by Lorentzian broadening.

	g ₁	g ₂	g ₃	g ₁ strain	g ₂ strain	g ₃ strain
as-prepared HKUST-1	1.98	1.94	2.44	0.60	0.59	0.65
250°C 1 h HKUST-1	2.14	2.13	2.37	0	0.47	0.72
250°C 3 h HKUST-1	2.19	2.12	2.40	0.05	0.31	0.73
250°C 10 h HKUST-1	2.19	2.10	2.49	0.04	0.26	0.63

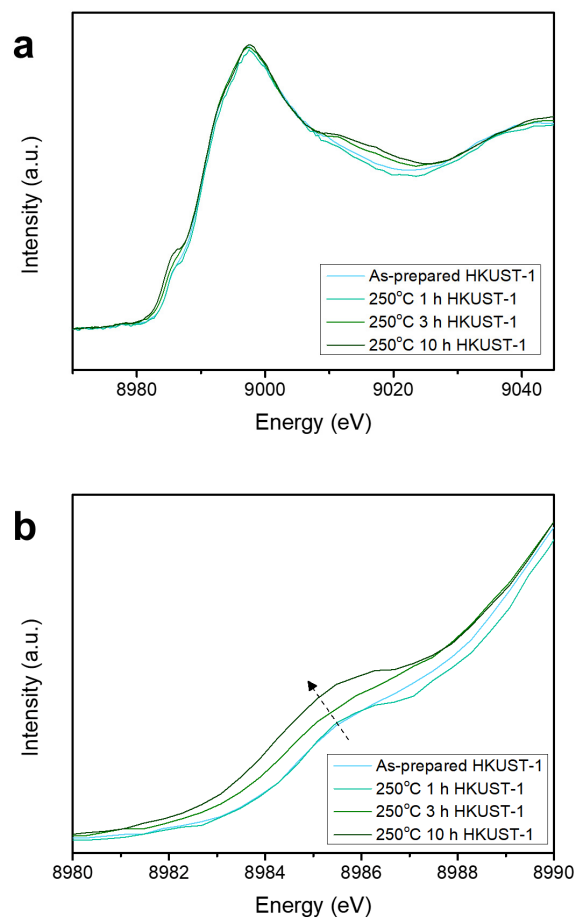


Figure S5. (a) XANES spectra of HKUST-1 to investigate the oxidation states of Cu according to the degree of thermal calcination. (b) Magnified XANES spectra which indicate the shoulder peak shift toward the lower energy. It reveals that 250°C calcination reduces the oxidation state of Cu in HKUST-1 compared to as-prepared HKUST-1.

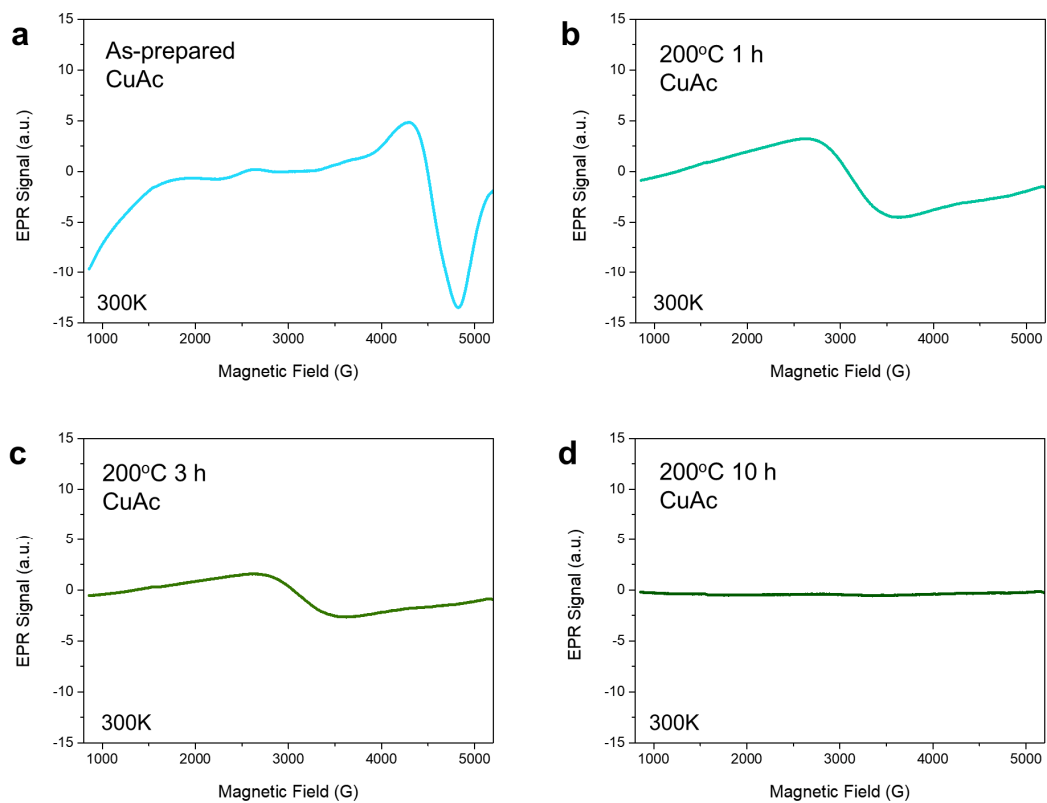


Figure S6. EPR analysis to investigate the effect of thermal calcination on the local atomic structures in paddle-wheel structured Cu dimer within CuAc. (a) as-prepared, (b) 200°C 1 h calcined, (c) 200°C 3 h calcined, and (d) 200°C 10 h calcined CuAc.

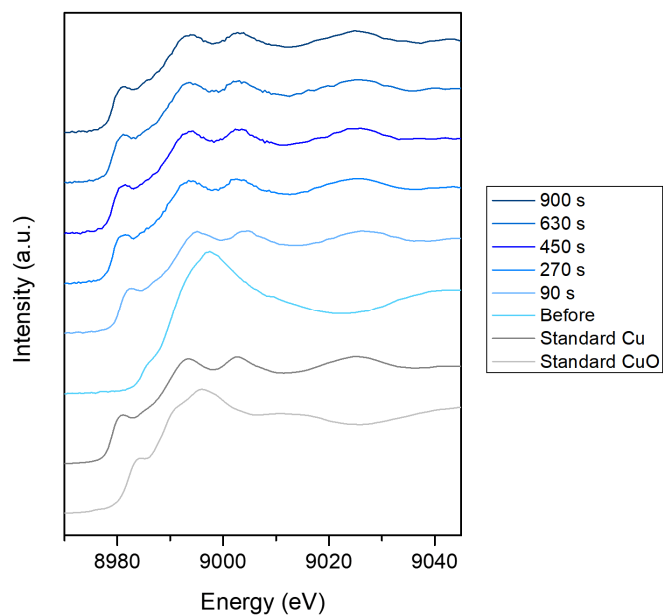


Figure S7. In situ XANES for real-time investigation of the Cu oxidation status in as-prepared HKUST-1 during the CO₂RR at constant -1.38 V vs. RHE (non-iR corrected) under 1M KOH.

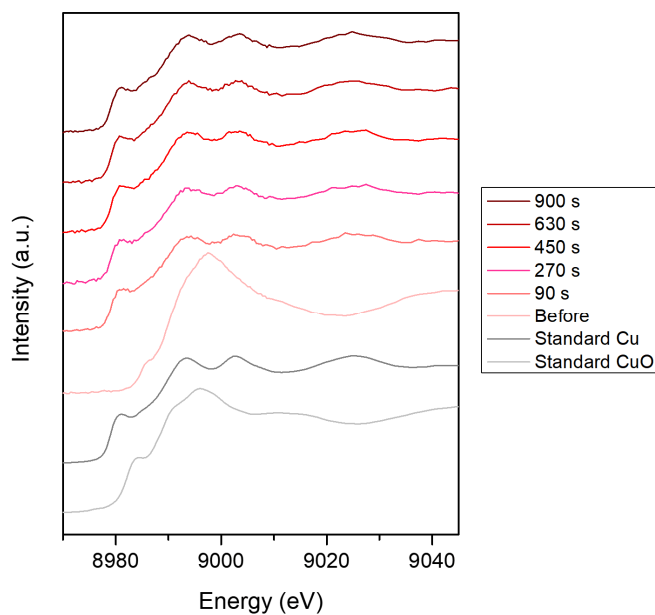


Figure S8. In situ XANES for real-time investigation of the Cu oxidation status in 250°C 1 h calcined HKUST-1 during the CO₂RR at constant -1.38 V vs. RHE (non-iR corrected) under 1M KOH.

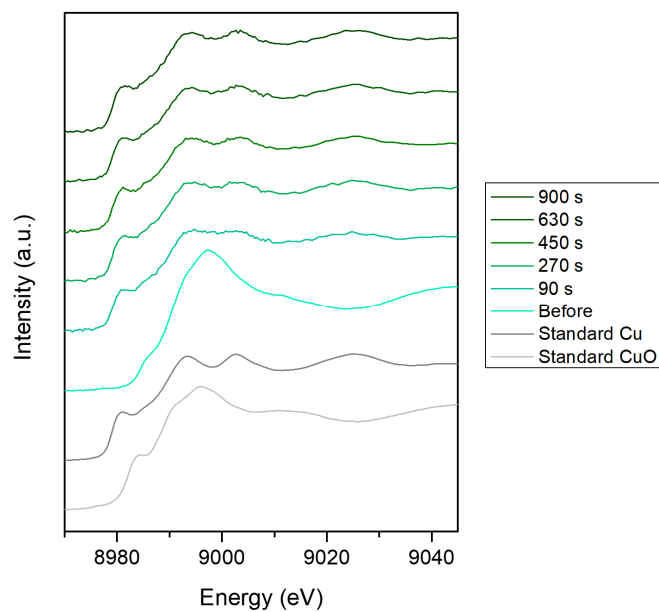


Figure S9. In situ XANES for real-time investigation of the Cu oxidation status in 250°C 3 h calcined HKUST-1 during the CO₂RR at constant -1.38 V vs. RHE (non-iR corrected) under 1M KOH.

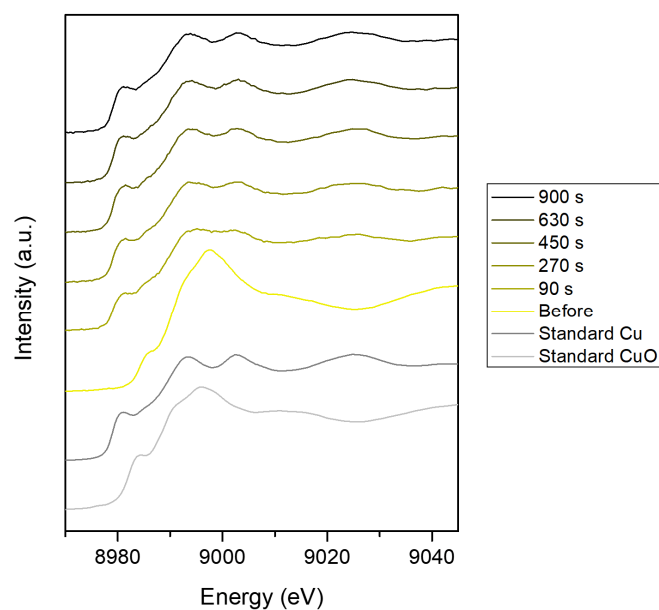


Figure S10. In situ XANES for real-time investigation of the Cu oxidation status in 250°C 10 h calcined HKUST-1 during the CO₂RR at constant -1.38 V vs. RHE (non-iR corrected) under 1M KOH.

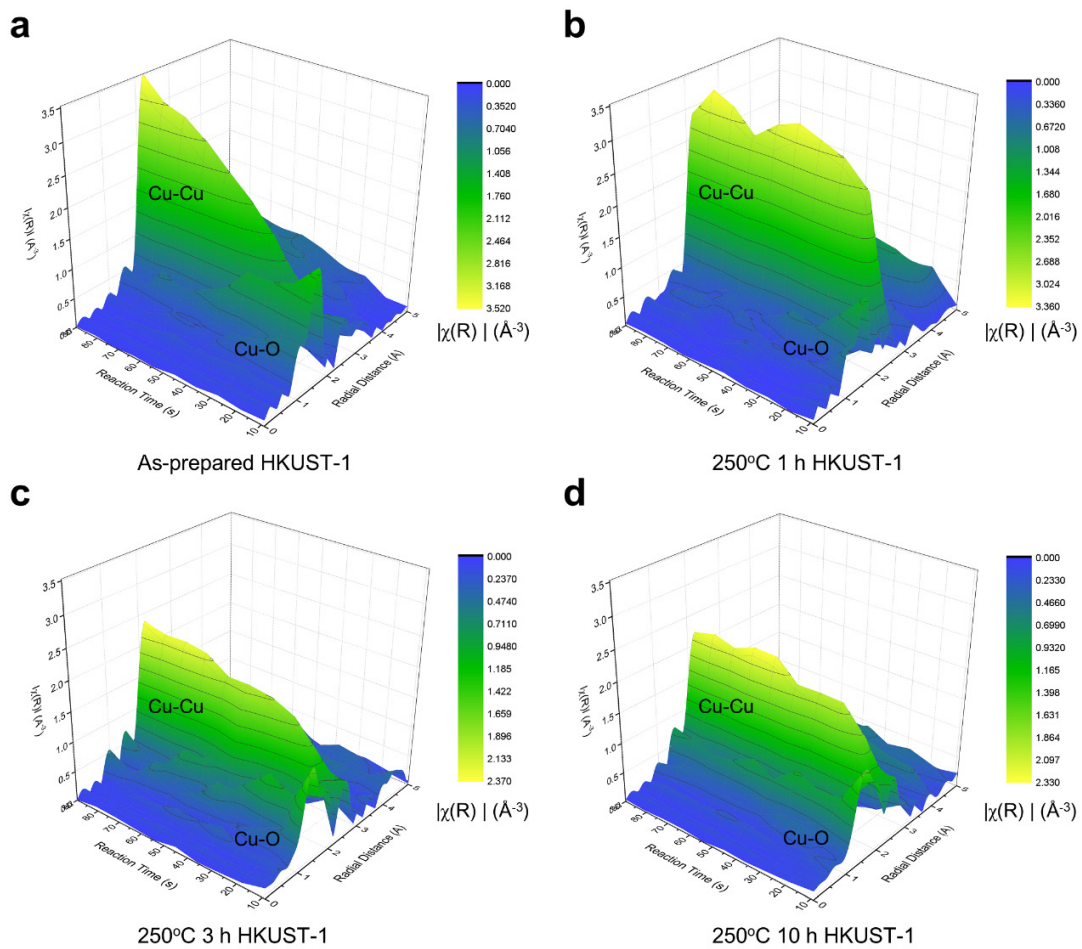


Figure S11. 3D map of in situ EXAFS according to the early stage reaction time in CO_2RR . (a) as-prepared HKUST-1, (b) 250°C 1 h calcined HKUST-1, (c) 250°C 3 h calcined HKUST-1, (d) 250°C 10 h calcined HKUST-1.

Table S3. Cu-Cu coordination numbers of HKUST-1 derived Cu clusters calculated from in situ EXAFS according to the reaction time of CO₂RR. (Coordination number of standard Cu foil= 12)

Reaction Time	as-prepared HKUST-1	250°C 1 h calcined HKUST-1	250°C 3 h calcined HKUST-1	250°C 10 h calcined HKUST-1
90 s	10.5393	11.3975	8.0345	8.9788
180 s	11.5521	11.3125	8.8754	9.6849
270 s	11.9126	9.7468	9.9182	10.0600
360 s	10.6983	9.7287	9.4984	11.1501
450 s	10.6377	10.5171	10.1437	10.0404
540 s	11.5757	10.4605	11.1739	10.3317
630 s	11.8778	10.0525	8.5456	10.8658
720 s	10.4030	10.5793	9.0722	11.1780
810 s	11.3428	11.5019	9.0988	11.7165
900 s	11.7446	11.5055	10.1983	10.9378

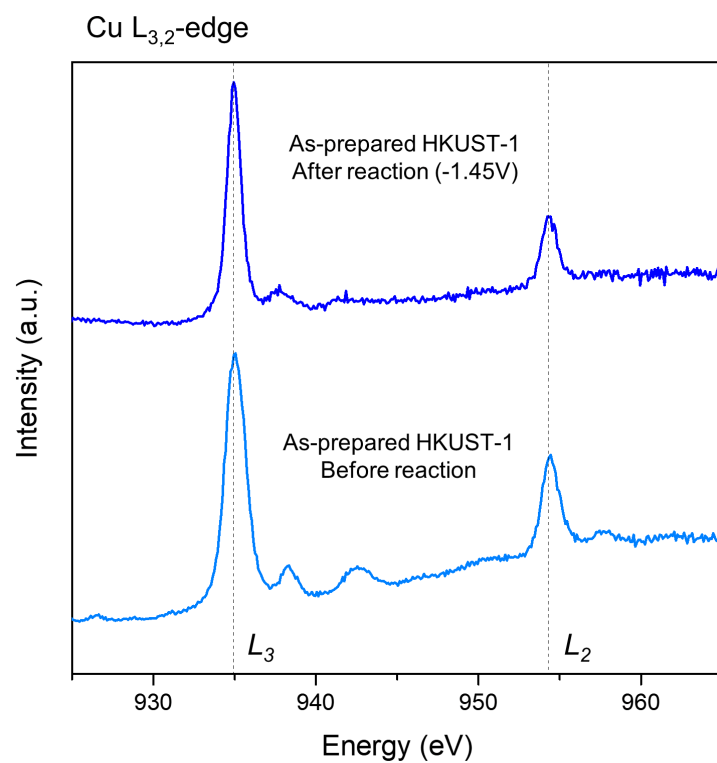


Figure S12. Ex situ soft-XAS for investigating the Cu oxidation status in as-prepared HKUST-1 after reaction. Comparing the Cu L_{3,2}-edge spectra of before and after the reaction showed same Cu oxidation number of 2+. It indicates that the size of Cu cluster formed by CO₂RR is very small enough to be easily oxidized.

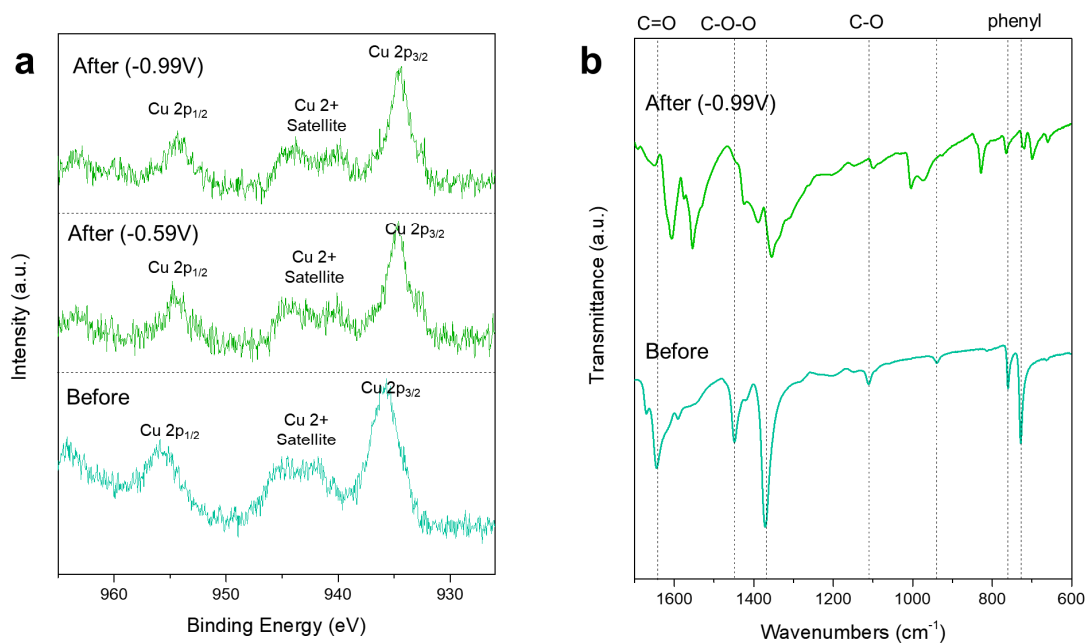


Figure S13. (a) Ex situ XPS based Cu oxidation status and (b) FT-IR based organic structure investigation of 250°C 1 h calcined HKUST-1 after CO₂RR. In XPS, the oxidation status of Cu in HKUST-1 was same in before and after reaction (-0.59 V, -0.99 V vs. RHE). FT-IR showed the formation of hydroxycarbonate functional group during CO₂RR.

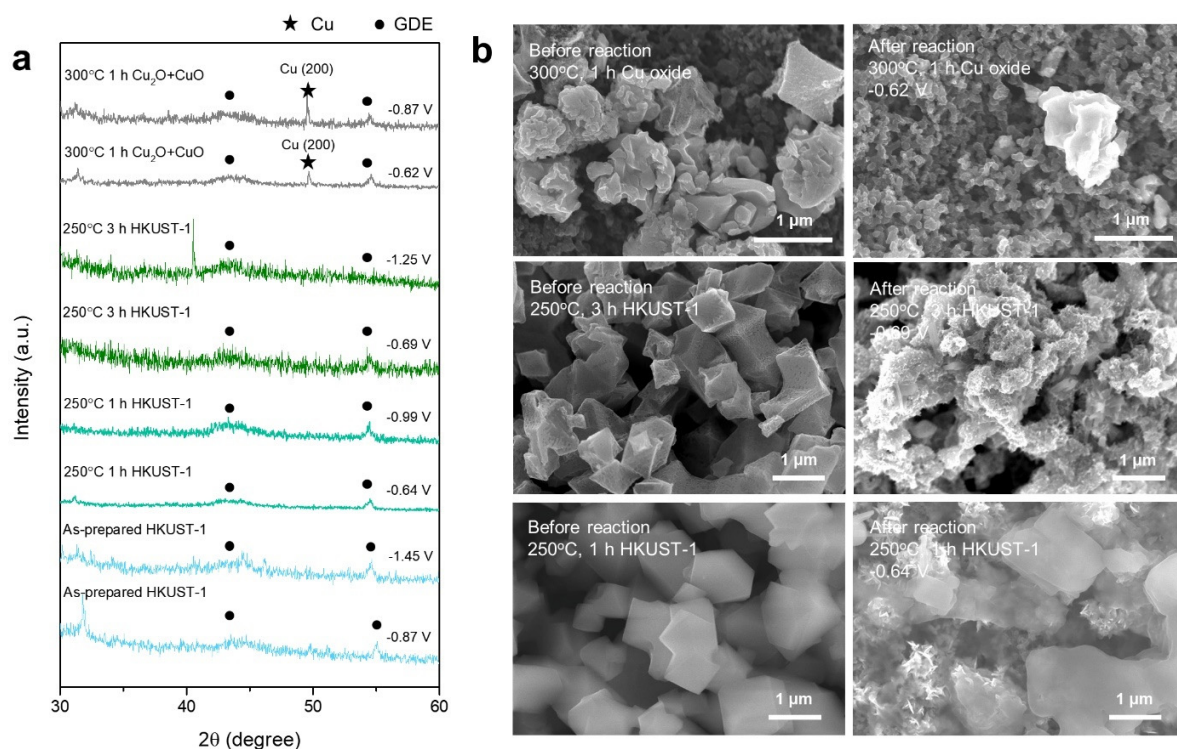


Figure S14. (a) XRD analysis to investigate the phase of HKUST-1 after CO₂RR according to the degree of calcination and applied potential in chronoamperometry. There was no Cu peak in the case of HKUST-1 (as-prepared, 250°C 1 h, 3 h calcination). However, in Cu oxide after 300°C 1 h calcination of HKUST-1, there was Cu peak after CO₂RR. (b) SEM images for investigating the structure change between before and after the reaction of HKUST-1 (250°C 1 h calcined HKUST-1 at -0.64 V vs. RHE, 250°C 3 h calcined HKUST-1 at -0.69 V vs. RHE, 300°C 1 h calcined HKUST-1 at -0.62 V vs. RHE).

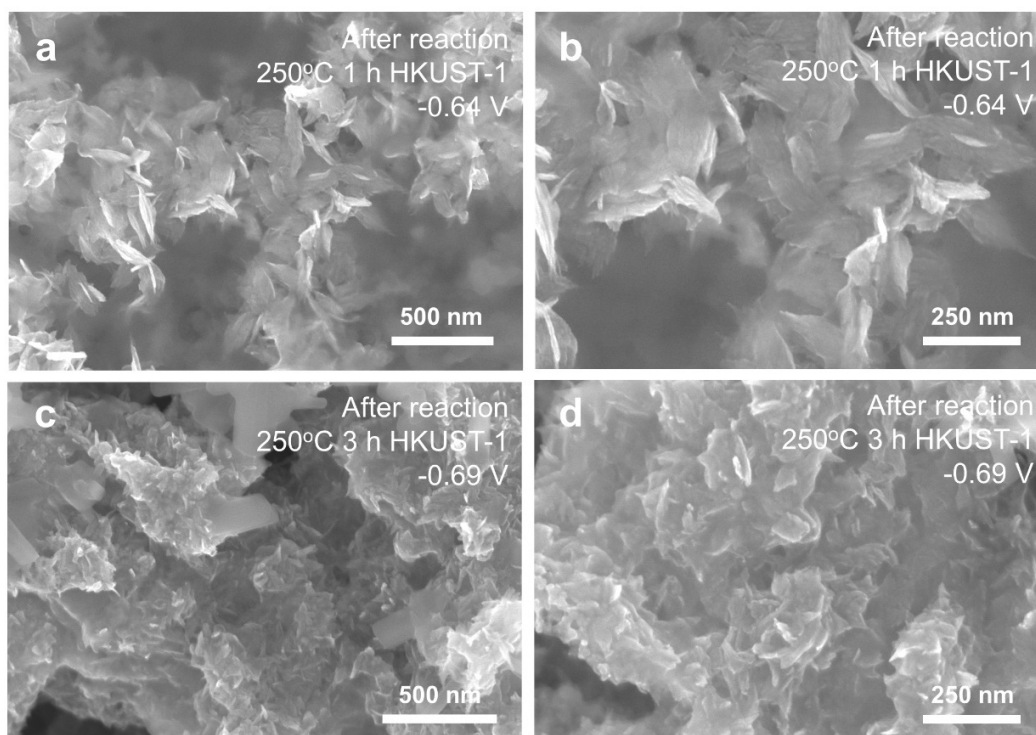


Figure S15. SEM images for investigating the structure after CO₂RR of HKUST-1. The 2D plate-like dendritic structures formed from HKUST-1 in both (a, b) 250°C 1 h calcination, and (c, d) 250°C 3 h calcination after CO₂RR. There was no Cu agglomeration which forms Cu nanoparticles.

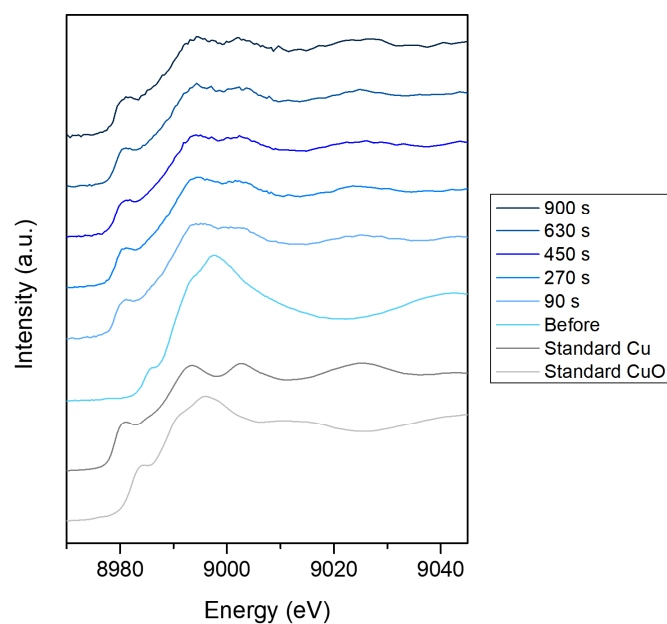


Figure S16. In situ XANES for real-time investigation of the Cu oxidation status in as-prepared CuAc during the CO₂RR at constant -1.38 V vs. RHE (non-iR corrected) under 1M KOH.

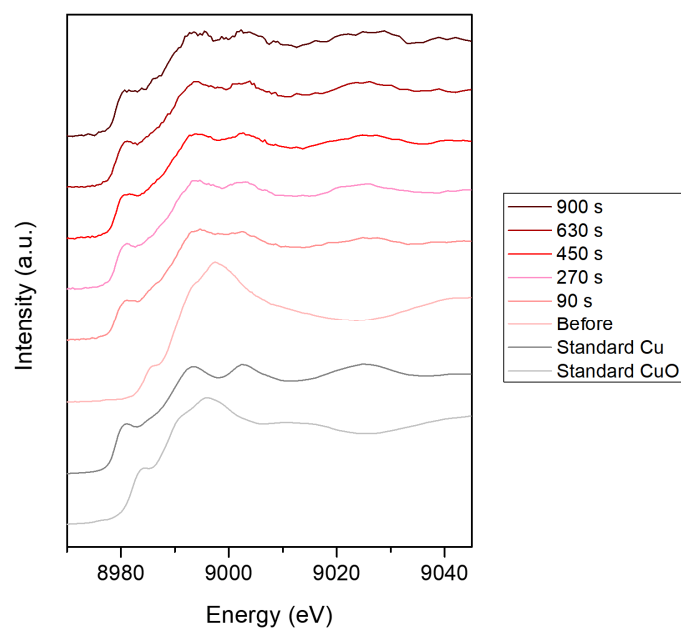


Figure S17. In situ XANES for real-time investigation of the Cu oxidation status in 200°C 1 h calcined CuAc during the CO₂RR at constant -1.38 V vs. RHE (non-iR corrected) under 1M KOH.

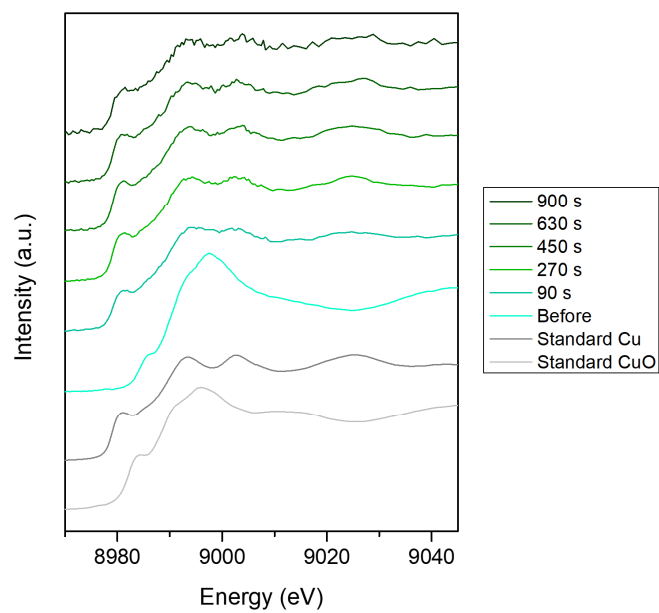


Figure S18. In situ XANES for real-time investigation of the Cu oxidation status in 200°C 3 h calcined CuAc during the CO₂RR at constant -1.38 V vs. RHE (non-iR corrected) under 1M KOH.

Table S4. Cu-Cu coordination numbers of CuAc derived Cu clusters calculated from in situ EXAFS according to the reaction time of CO₂RR. (Coordination number of standard Cu foil= 12)

Reaction Time	as-prepared CuAc	200°C 1 h calcined CuAc	200°C 3 h calcined CuAc
90 s	9.3834	9.2948	9.5663
180 s	8.6293	9.9868	10.7435
270 s	9.2360	11.0185	10.1615
360 s	9.2519	9.6284	10.3833
450 s	9.5292	9.8109	10.9788
540 s	8.8856	10.8251	11.8055
630 s	9.7331	11.0343	10.0931

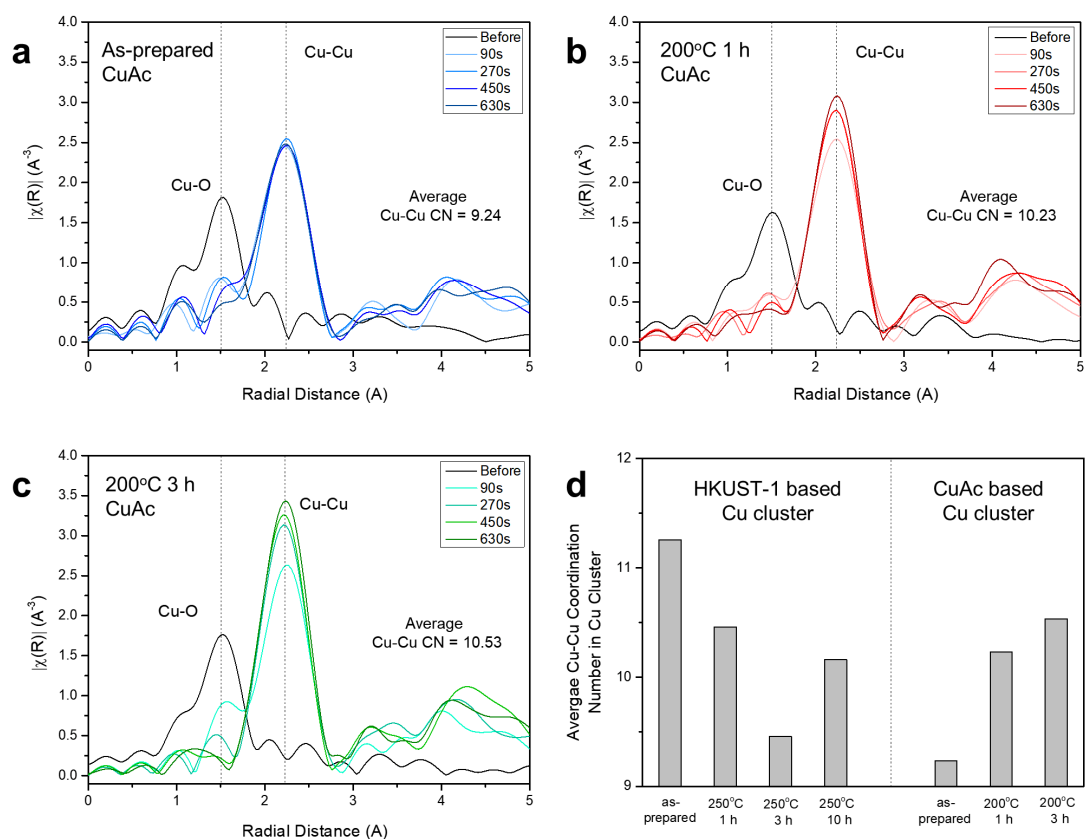


Figure S19. In-situ EXAFS for tracking the real-time atomic structure of CuAc derived Cu clusters during CO₂RR. EXAFS spectra were scanned according to the reaction time at the constant potential of -1.38 V vs. RHE (non-iR corrected) in 1M KOH, each spectrum was collected with a duration of 9 s. (a) as-prepared CuAc, (b) 200°C 1 h calcined CuAc, (c) 200°C 3 h calcined CuAc. (d) Comparison of average Cu-Cu coordination number of Cu clusters formed from HKUST-1 (surface structure effect) and CuAc (size effect) according to the calcination condition.

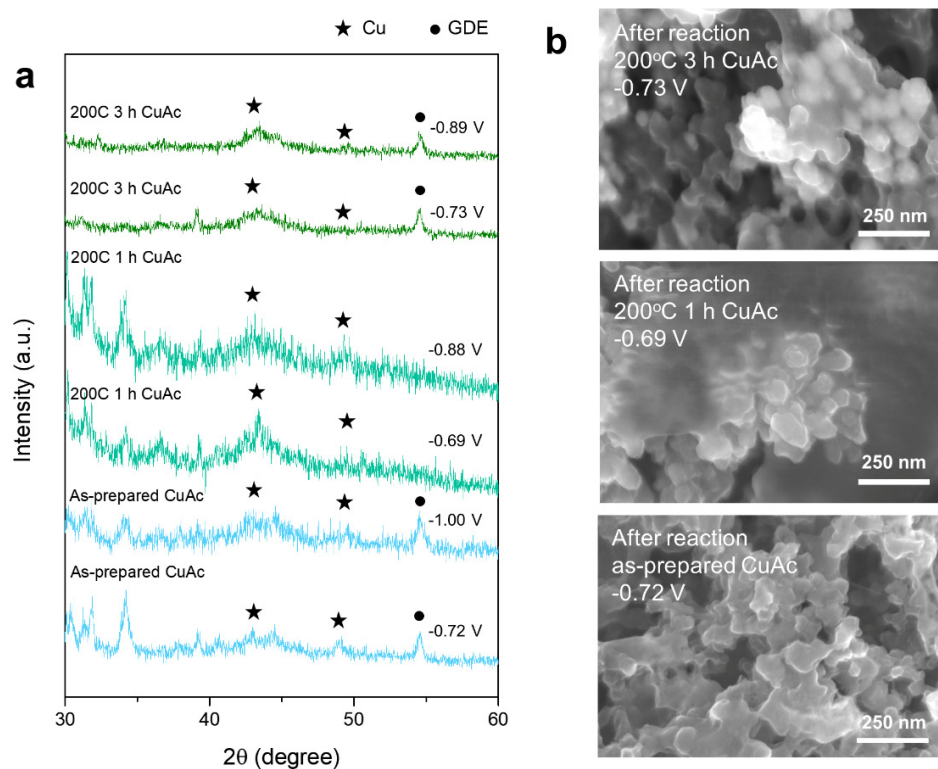


Figure S20. (a) XRD analysis to investigate the phase of CuAc after CO₂RR according to the degree of calcination and applied potential for chronoamperometry. Crystalline Cu XRD peaks were generated in CuAc unlike HKUST-1. (b) SEM images after the CO₂RR of CuAc. Agglomerated Cu nanoparticles formed from as-prepared CuAc at -0.72 V vs. RHE, 200°C 1 h calcined CuAc at -0.69 V vs. RHE, and the 200°C 3 h calcined CuAc at -0.73 V vs. RHE.

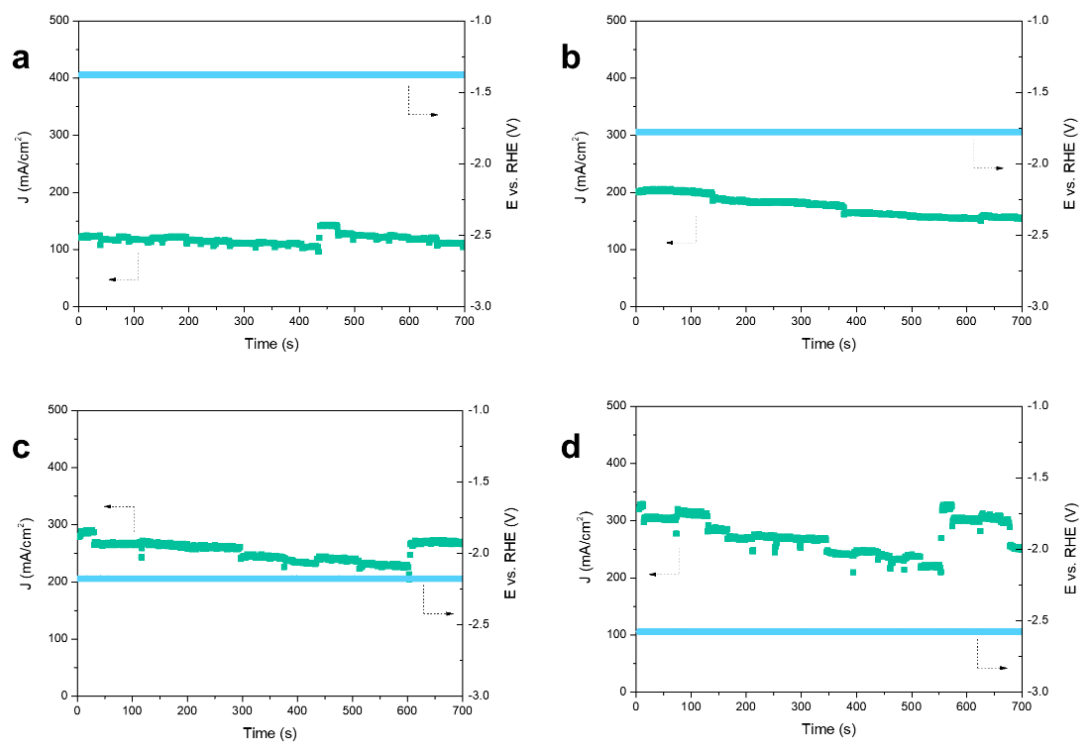


Figure S21. Chronoamperometry of as-prepared HKUST-1 at 1M KOH according to the applied RHE potential of (a) -1.38 V, (b) -1.78 V, (c) -2.18 V, and (d) -2.58 V (non- iR corrected).

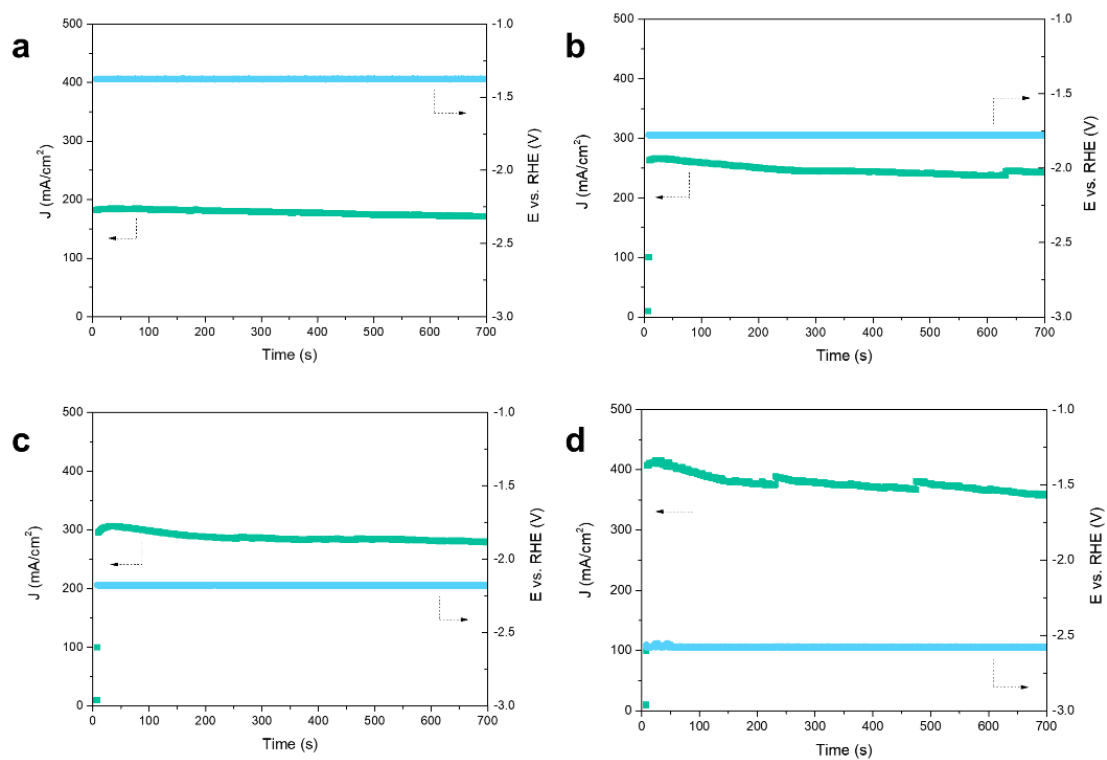


Figure S22. Chronoamperometry of 250°C 1 h calcined HKUST-1 at 1M KOH according to the applied RHE potential of (a) -1.38 V, (b) -1.78 V, (c) -2.18 V, and (d) -2.58 V (non-iR corrected).

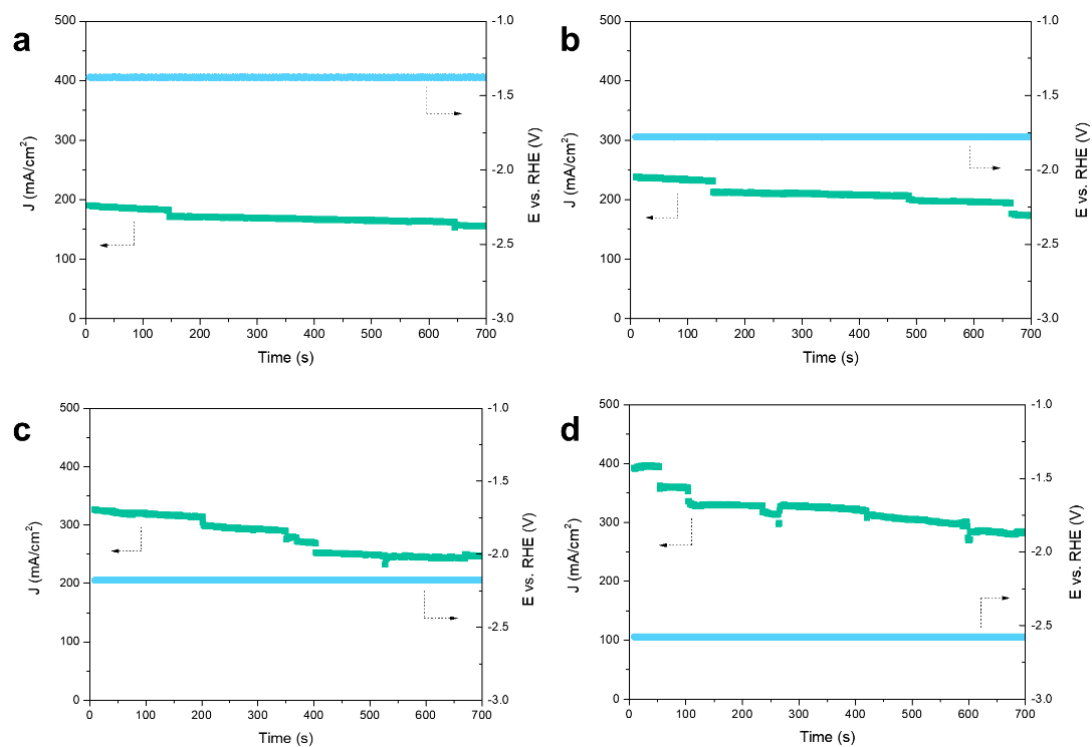


Figure S23. Chronoamperometry of 250°C 3 h calcined HKUST-1 at 1M KOH according to the applied RHE potential of (a) -1.38 V, (b) -1.78 V, (c) -2.18 V, and (d) -2.58 V (non- iR corrected).

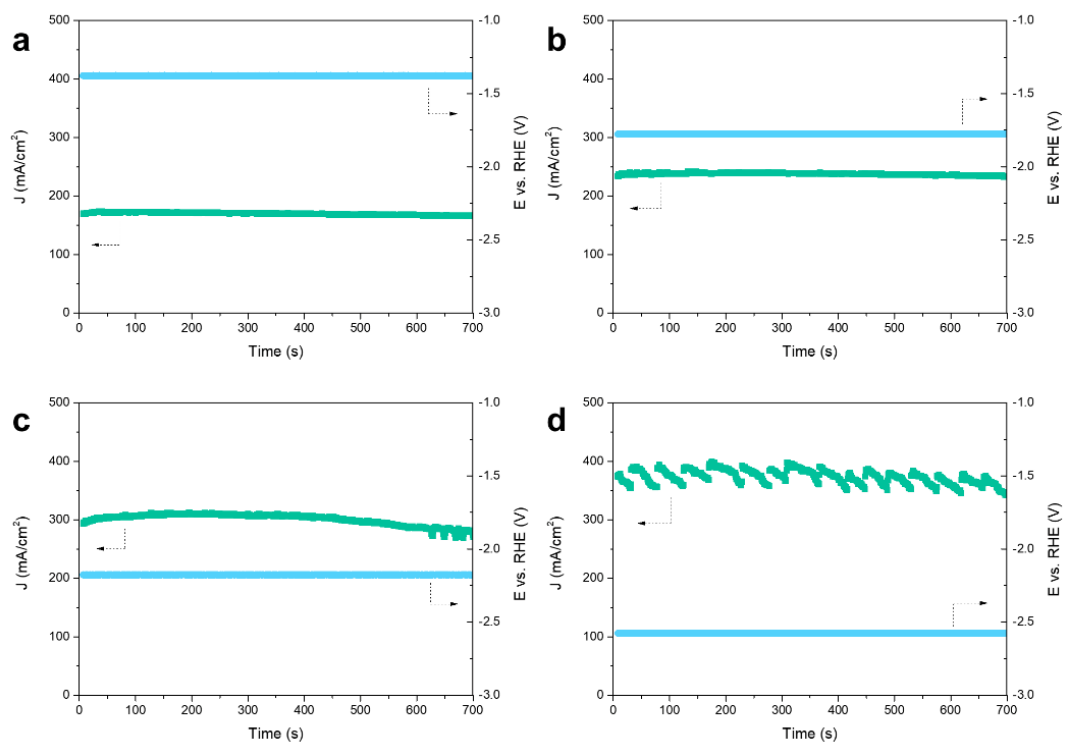


Figure S24. Chronoamperometry of 250°C 10 h calcined HKUST-1 at 1M KOH according to the applied RHE potential of (a) -1.38 V, (b) -1.78 V, (c) -2.18 V, and (d) -2.58 V (non- iR corrected).

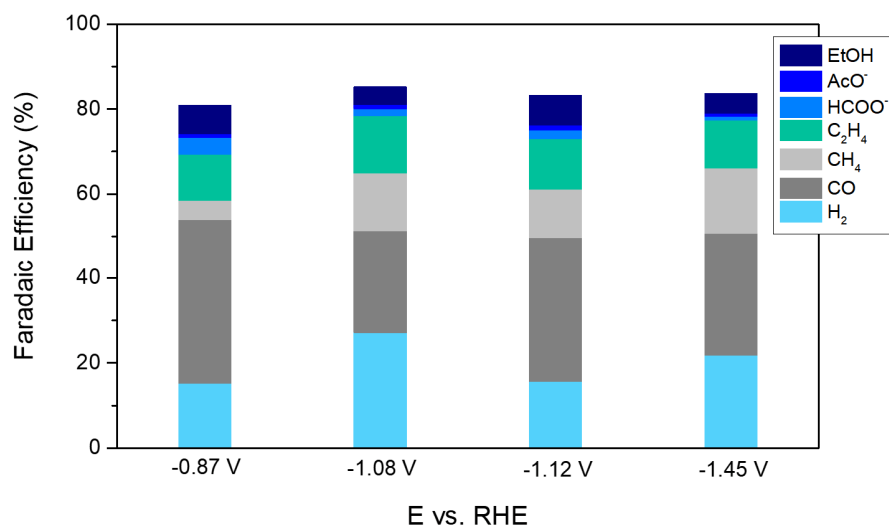


Figure S25. Gas and liquid products analysis with Faradaic efficiency according to the applied potential of CO₂RR in as-prepared HKUST-1.

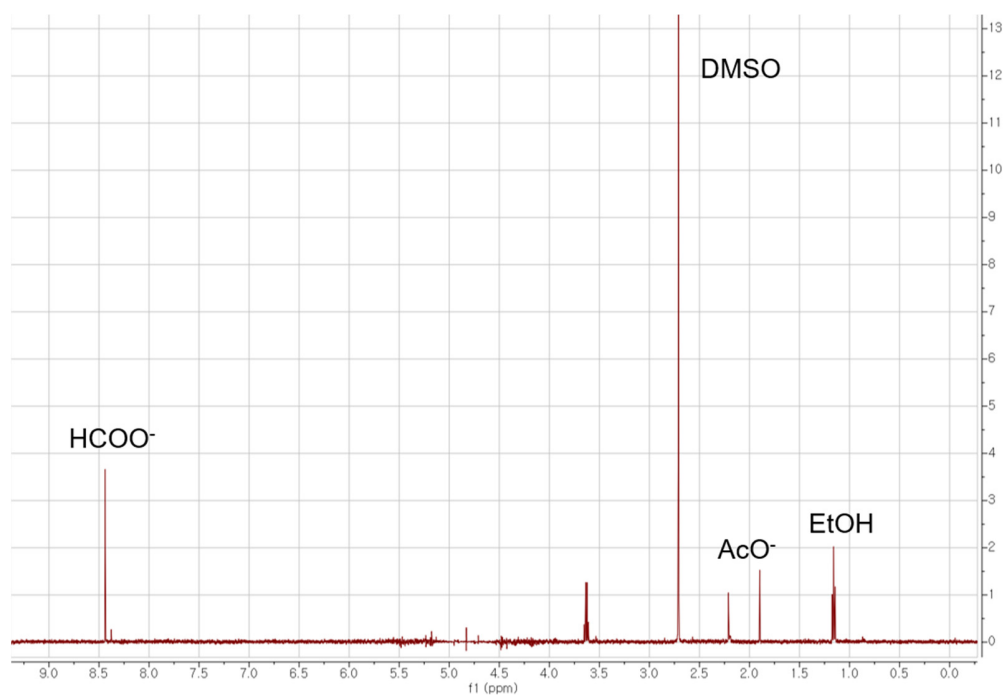


Figure S26. NMR for liquid product analysis of CO₂RR in as-prepared HKUST-1

Table S5. CO₂RR activity and product comparison of Cu based organometallic and MOF catalysts.

Initial Material	Voltage	Current	Product FE of CO ₂ RR	Electrolyte	Reference
[Organometallic] Cu porphyrin	-0.976 V (RHE)	49 mA/cm ²	C ₂ H ₄ (17%) + CH ₄ (27%)+ CO (10%)	0.5M KHCO ₃	<i>Z. Weng, et al., J. Am. Chem. Soc., 138, 26 (2016)</i> ¹
[Organometallic] Cu phthalocyanine	-1.7 V (Ag/AgCl)	40 mA/cm ²	C ₂ H ₄ (25%) + CO (5%) + CH ₄ (5%)	0.5M KCl	<i>S. Kusama, et al., ACS Catal., 7, 12 (2017)</i> ²
[Organometallic] Cu phthalocyanine + CNT	-1.06 V (RHE)	21 mA/cm ²	CH ₄ (66%) + H ₂ (34%)	0.5M KHCO ₃	<i>Z. Weng, et al., Nat. Comm., 9, 415 (2018)</i> ³
[Organometallic] Cu(cyclam)Cl ₂ +CNT	-1.06 V (RHE)	8 mA/cm ²	CO (3%) + H ₂ (91%)	0.5M KHCO ₃	<i>Z. Weng, et al., Nat. Comm., 9, 415 (2018)</i> ³
Cu NPs embedded NU-1000 (Zr MOF)	-0.82 V (RHE)	1.8 mA/cm ²	HCOO ⁻ (30%) + CO (5%) + H ₂ (65%)	0.1M NaClO ₄	<i>C.-W. Kung, et al., ACS Energy Lett., 2, 10 (2017)</i> ⁴
HKUST-1	-0.9 V (Ag/AgCl)	10 mA/cm ²	C ₂ H ₅ OH (10.3%) + CH ₃ OH (5.6%)	0.5M KHCO ₃	<i>J. Albo, et al., ChemSusChem, 10 (2017)</i> ⁵
HKUST-1 + Cu nanoparticle	-2.0 V (SCE)	20 mA/cm ²	C ₂ H ₄ (12%) + CH ₄ (19%) + H ₂ (55%)	0.5M NaHCO ₃	<i>Y.-L. Qui, et al., ACS Appl. Mater. Interfaces, 10, 3 (2018)</i> ⁶
HKUST-1 + CNT	-1.06 V (RHE)	8 mA/cm ²	CH ₄ (25%) + CO (5%) + H ₂ (60%)	0.5M KHCO ₃	<i>Z. Weng, et al., Nat. Comm., 9, 415 (2018)</i> ³
Cu dimer distorted HKUST-1	-1.07 V (RHE)	262 mA/cm²	C₂H₄ (45%) + CO (24%) + H₂ (7%) + CH₄ (0.4%)	1M KOH	This work

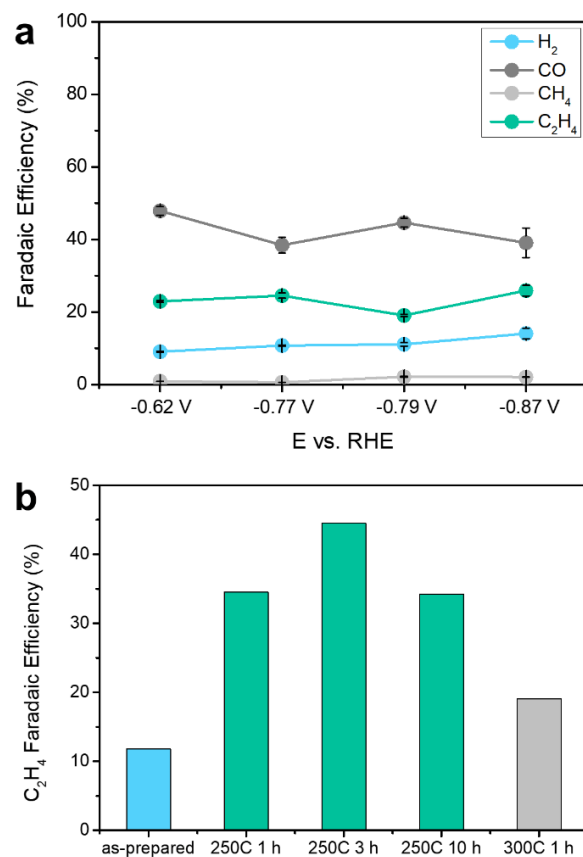


Figure S27. (a) CO₂RR gaseous products of 300°C 1 h calcined Cu oxide formed by combustion of HKUST-1 according to the applied potential. (b) C₂H₄ FE comparison between as-prepared HKUST-1 (light blue), 250°C calcined HKUST-1 (green), 300°C calcined Cu oxide from HKUST-1 combustion (gray).

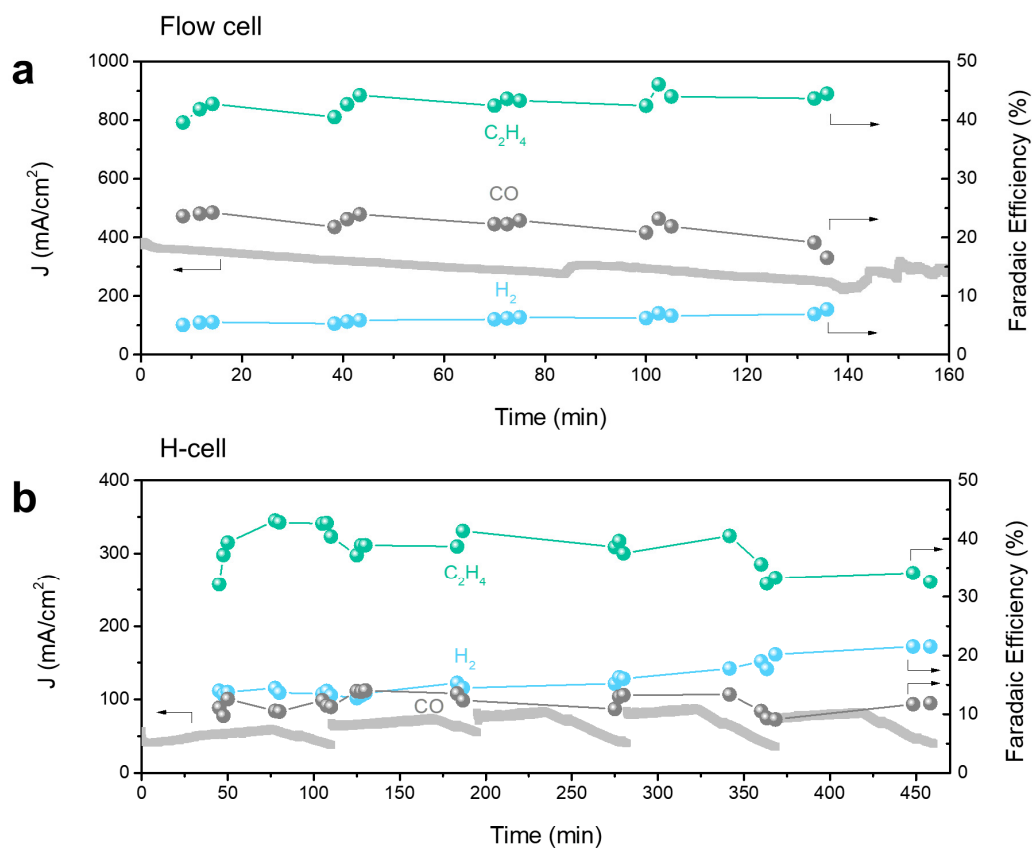


Figure S28. CO₂RR stability measurement with chronoamperometry of 250°C 3 h calcined HKUST-1 in (a) flow cell and (b) H-cell. 1M KOH was used as an electrolyte and the potential of -3.2 V vs. Ag/AgCl (-2.2 V vs. RHE, non-iR corrected) was applied for flow cell operation. 0.1M KHCO₃ was used as an electrolyte and the potential of -2.4 V vs. Ag/AgCl (-1.8 V vs. RHE, non-iR corrected) was applied for H-cell.

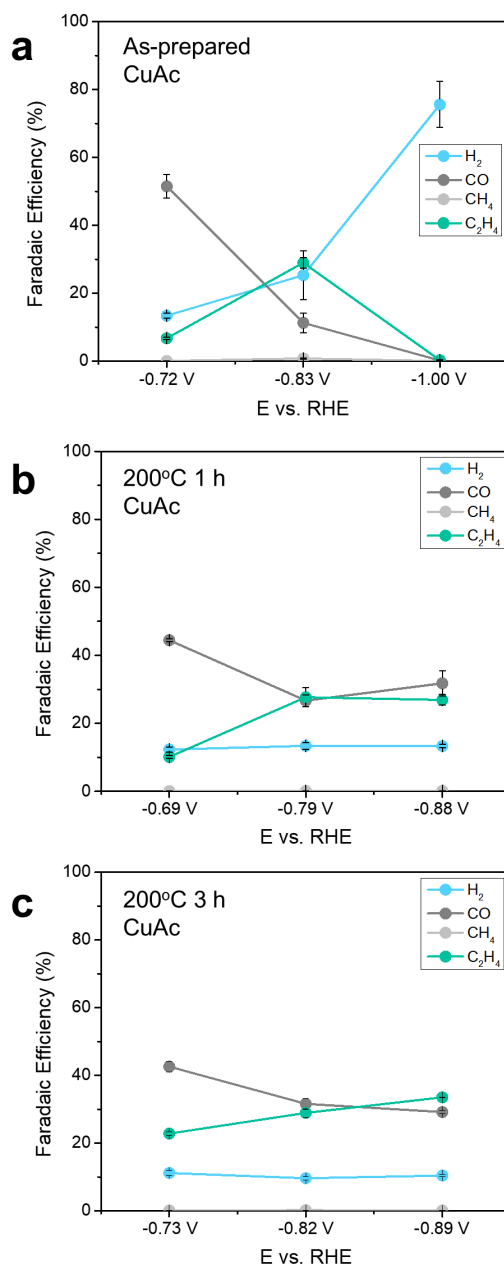


Figure S29. Investigation of CO₂RR activity and product Faradaic efficiency at 1M KOH according to the applied potential of (a) as-prepared CuAc, (b) 200°C 1 h calcined CuAc, (c) 200°C 3 h calcined CuAc. The same E vs. RHE was applied as -1.38, -1.78, and -2.18 V (non iR corrected).

References

- (1) Weng, Z.; Jiang, J.; Wu, Y.; Wu, Z.; Guo, X.; Materna, K. L.; Liu, W.; Batista, V. S.; Brudvig, G. W.; Wang, H. *J. Am. Chem. Soc.* **2016**, *138*, 8076–8079.
- (2) Kusama, S.; Saito, T.; Hashiba, H.; Sakai, A.; Yotsuhashi, S. *ACS Catal.* **2017**, *7*, 8382–8385.
- (3) Weng, Z.; Wu, Y.; Wang, M.; Jiang, J.; Yang, K.; Huo, S.; Wang, X.-F.; Ma, Q.; Brudvig, G. W.; Batista, V. S.; Liang, Y.; Feng, Z.; Wang, H. *Nat. Commun.* **2018**, *9*, 415.
- (4) Kung, C.-W.; Audu, C. O.; Peters, A. W.; Noh, H.; Farha, O. K.; Hupp, J. T. *ACS Energy Lett.* **2017**, *2*, 2394–2401.
- (5) Albo, J.; Vallejo, D.; Beobide, G.; Castillo, O.; Castaño, P.; Irabien, A. *ChemSusChem* **2016**, *10*, 1100–1109.
- (6) Qiu, Y.-L.; Zhong, H.-X.; Zhang, T.-T.; Xu, W.-B.; Su, P.-P.; Li, X.-F.; Zhang, H.-M. *ACS Appl. Mater. Interfaces* **2018**, *10*, 2480–2489.
- (7) Dinh, C.-T.; Burdyny, T.; Kibria, M. G.; Seifitokaldani, A.; Gabardo, C. M.; García de Arquer, F. P.; Kiani, A.; Edwards, J. P.; De Luna, P.; Bushuyev, O. S.; Zou, C.; Quintero-Bermudez, R.; Pang, Y.; Sinton, D.; Sargent, E. H. *Science* **2018**, *360*, 783–787.